Research Article

Collimated Magnetron Sputter Deposition for Mirror Coatings

**Anette Vickery,[1] Carsten P. Jensen,[2] Finn E. Christensen,[2]
Mads Peter Steenstrup,[3] and Troels Schønfeldt[3]**

[1] *Nano-Science Center, University of Copenhagen, The H. C. Ørsted Institute, Universitetsparken 5,
2100 Copenhagen, Denmark*
[2] *Danish National Space Center, Juliane Maries Vej 30, 2100 Copenhagen, Denmark*
[3] *Niels Bohr Institute, University of Copenhagen, The H. C. Ørsted Institute, Universitetsparken 5,
2100 Copenhagen, Denmark*

Correspondence should be addressed to Anette Vickery, anette@vickery.dk

At the Danish National Space Center (DNSC), a planar magnetron sputtering chamber has been established as a research and production coating facility for curved X-ray mirrors for hard X-ray optics for astronomical X-ray telescopes. In the following, we present experimental evidence that a collimation of the sputtered particles is an efficient way to suppress the interfacial roughness of the produced multilayer. We present two different types of collimation optimized for the production of low roughness curved mirrors and flat mirrors, respectively.

1. Introduction

Multilayers play an important role in X-ray optics and are used in a variety of applications including synchrotron radiation, free electron lasers (FELs), medical optics, and space-borne X-ray telescopes. The fabrication of multilayers requires high precision of the layer thickness not only in the growth direction but also laterally to obtain the desired uniformity or the thickness gradient with respect to a given application. Further the specular intensity reflectivity of the multilayer decreases exponentially with the sum of the squared magnitude of the interface roughness and the interfacial diffusion.

At the Danish National Space Center (DNSC), a planar DC-magnetron sputtering chamber has been established as a research and production coating facility for curved X-ray mirrors for hard X-ray optics for astronomical X-ray telescopes including the HEFT telescopes [1] and the forthcoming NuSTAR telescopes [2, 3]. This means that this sputtering facility has been dedicated solely to the production of laterally homogeneous mirrors with radii of curvature in the range 60–120 mm. For this reason, the production of long (≈200 mm) flat mirrors for, that is, synchrotron radiation or FEL optics has not been an option at this facility. However by a minor change of the coating setup, the sputtering facility has now been qualified also for production of such mirrors. The first flat homogeneous mirrors produced at DNSC are used in the focusing optics for the new compact light source [4] to be installed at Copenhagen University. The X-ray telescope mirrors typically have several hundred bilayers with individual bilayer thicknesses as low as 1.5 nm. Further it is proposed that the capabilities of DNSC are used for developing X-ray optics for the European X-ray free electron laser (XFEL) which will be built at the DESY site in Hamburg with first operation planned in 2013.

In the following, we present experimental evidence that a collimation of the sputtered particles is an efficient way to suppress the interfacial roughness of the produced multilayer. We present two different types of collimation optimized for the production of homogeneous curved mirrors and flat mirrors, respectively.

All multilayers presented in this paper has been produced at DNSC using DC-magnetron sputtering. The substrates are commercially available Si wafers with an rms roughness of about 2.5 Å. The rms roughness of the multilayers has been determined by measurements of the specular X-ray intensity reflectivity at Cu K_α radiation (8.05 keV).
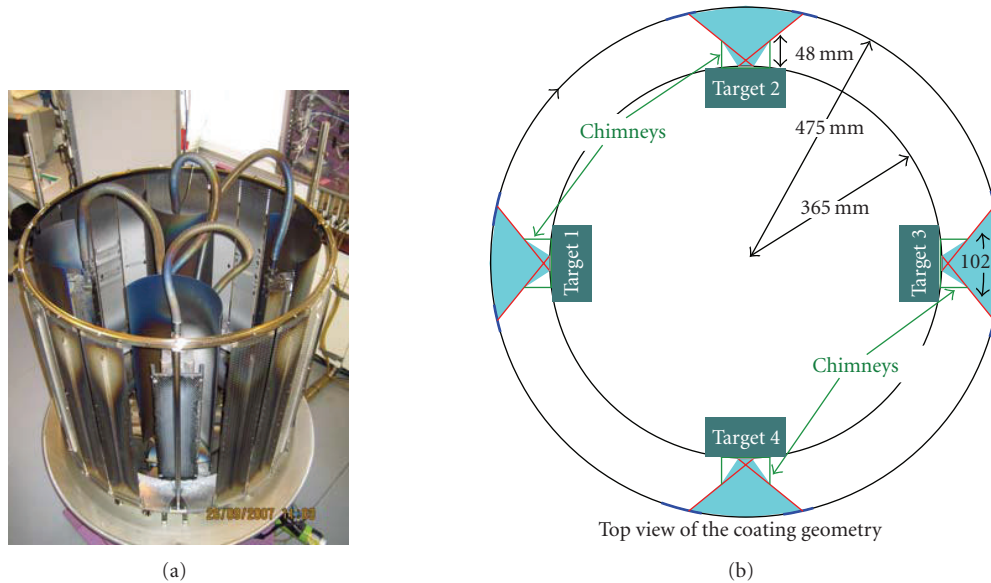
(a)

(b)

FIGURE 1: (a) The sputtering chamber seen from above. (b) A top-view sketch of the coating geometry. In the horizontal plane the opening angle of each target is limited by a *chimney* to approximately 102°.

2. The Sputtering Chamber

The coating facility at DNSC is optimized to make multilayer coatings that meet strict quality requirements for hard X-ray optics and on the same time have a high throughput: it is possible to coat up to 0.8 m^2 per run.

Figure 1 shows a photograph of the inside of the magnetron sputtering chamber at DNSC and a top-view sketch of the coating geometry. The facility is a bell-jar vacuum chamber with a diameter of 1 m and it is 1.2 m tall. The 4 DC-magnetron sources (the targets) with shutters are positioned inside the sample carrousel, facing out toward the substrates. On the photography, two shutters are opened while the remaining two are closed. The substrates are mounted vertically on the mounting plates of the big sample carrousel so the coating geometry is cylindrical. There are a total of 18 mounting plates, each 800 mm tall and 125 mm wide and 3 open slots. The presence of the open slots is to prevent sputtering the substrate when opening and closing the shutters and accelerating the ring to the desired speed. The coating rate is strongly dependent on the distance between the target and the substrate. Therefore, to ensure a reproducible lateral homogeneity of the produced multilayers, the alignment of the mounting plates is strictly controlled: the bottom of the mounting plates are fixed by narrow slots on the sample carousel while the top of the mounting plates are constrained by a steel ring with the same diameter.

During the coating, the targets remain stationary and when a target shutter is open, material is deposited onto the substrates passing by. When the coating parameters, Ar pressure, and applied power to the cathodes have been decided upon, the thickness of each of the materials is controlled by the rotation speed of the sample carrousel.

When producing multilayers comprised of two different materials normally three of the four magnetron sources are in operation, so that two of three targets in operation are equipped with the same material.

3. The Collimation of the Sputtered Particles

Here, we present experimental evidence that for the DC-magnetron sputtering facility at DNSC, the collimation of the sputtered material is essential in order to suppress the interface roughness of the deposited multi-layers. We present two different types of collimators, one which is suitable for the coating of strongly curved mirrors (radii of curvature in the range 60–120 mm) and another one suitable for the coating of flat mirrors. In the following, the types of collimation are referred to as the *separator-plate collimation* and the *honeycomb collimation*, respectively.

3.1. Separator-Plate Collimation

3.1.1. Experimental Setup

Figure 2(a) shows one curved substrate mounted on a mounting plate between two *separator plates*. The role of the separator plates is to provide a collimation of the sputtered particles, as explained in the sketch shown in Figure 2(b). This is a side-view sketch of one target and a substrate during coating. The target is standing vertical and the arrows symbolize the particles ejected from the target on their way to the substrate shown to the right. The horizontal lines indicate the separator plates which provide the collimation and prevent the material symbolized with the red arrows from reaching the (flat) substrate. The degree of collimation in the vertical direction is described by the opening angle β of
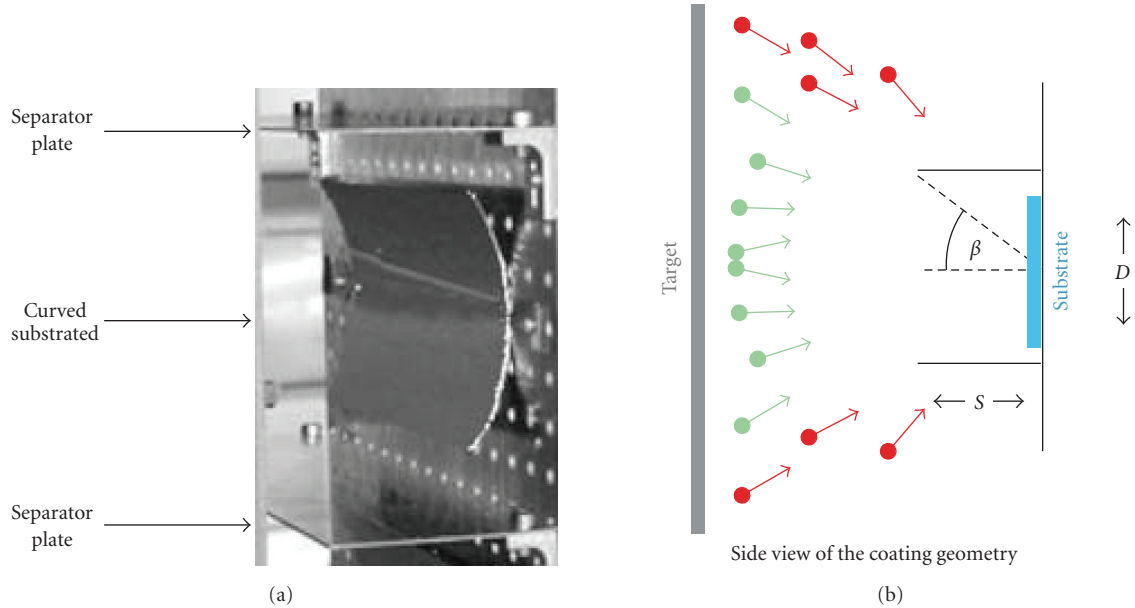
FIGURE 2: (a) Two separator plates and one curved substrate. The width of the separator plate (S in the sketch below) is 50 mm. (b) For clarity, in this side-view sketch, the chimney around the target has been left out. The dimensions of the sputtering chamber limits the maximum width of the separator plates to $S = 62$ mm.

the collimator. In the horizontal direction, the total opening angle of the chimney around the target is $\pm 51°$.

3.1.2. Experiment I

For 4 different pressures of Ar in the chamber, sets of multilayers comprised of 10 bilayers of W/Si have been produced with different separator plate distances (D in Figure 2(b)). All other parameters are fixed. The bilayer thickness, the fraction of Si in the multilayer, and the rms roughness have been determined from the measurements of the specular intensity reflectivity at Cu K$_\alpha$ radiation. The results of the measurements are shown in Figure 3. From these data, it can be seen that the coating rate of W is independent of the Ar pressure and the degree of collimation. In contrast to this, the Si coating rate decreases with increasing Ar pressure and with increasing degree of collimation. We interpret this to be an effect of gas scattering: it is expected that there will be some scattering of the sputtered material on the Ar atoms. The mass of an Si atom amounts to only 70% of that of Ar, so the paths of the Si atoms from the target to the substrate are likely to be affected by scattering. This is in contrast to the W atom, the mass of which is more than 4 times that of the Ar atom. This theory is supported by the data presented in Figure 3(c): a decrease of the Ar pressure leads to an increase of Γ_{Si}, that is, the scattering of the Si atoms on the Ar ions is less pronounced the lower the Ar pressure. In [5], Rossnagel et al. report on similar results for the deposition rate of collimated magnetron sputtering. Turning toward the view-graph D, we see that for a given collimation the observed rms roughness increases with increasing Ar pressure. Further it is clear that

an increase of the angle β also leads to an increase of the rms roughness.

For curved X-ray telescope mirrors, the collimation has been successfully provided by the *separator plates* [1]. The geometry of the sputtering chamber limits the width of the separator plates to 62 mm, so for $\beta = 50°$ the maximum space between the separator plates is $D = 147$ mm. This in turn limits the length of the substrates in the vertical direction and the cylindrical coating geometry limits the dimensions of the substrates in the horizontal direction. However, regarding the coating of flat multilayer mirrors, the most severe problem is that the separator plates induce a strong variation of the coating rate along the length of the substrate (from now on referred to as *the shadowing effect*): experiments with $D = 140$ mm and $S = 50$ mm have shown that 50 mm from the center of the substrate (i.e., toward the ends of the substrate close to the separator plates), the coating rate has decreased with 15%. It is worth noting that the shadowing effect is beneficial when coating curved samples: due to the cylindrical coating geomtry, the edges of one curved sample are closer to the target than the center of the sample. Therefore, without the shadowing effect, the thickness of the deposited layer would increase dramatically towards the edges of the sample, since the edges are relatively close to the target [1].

3.2. The Honeycomb Collimation

3.2.1. Experimental Setup

Figure 4(left) shows a sketch of a honeycomb mesh. Figures 4(a) and 4(b) show side- and top-view sketches of one target
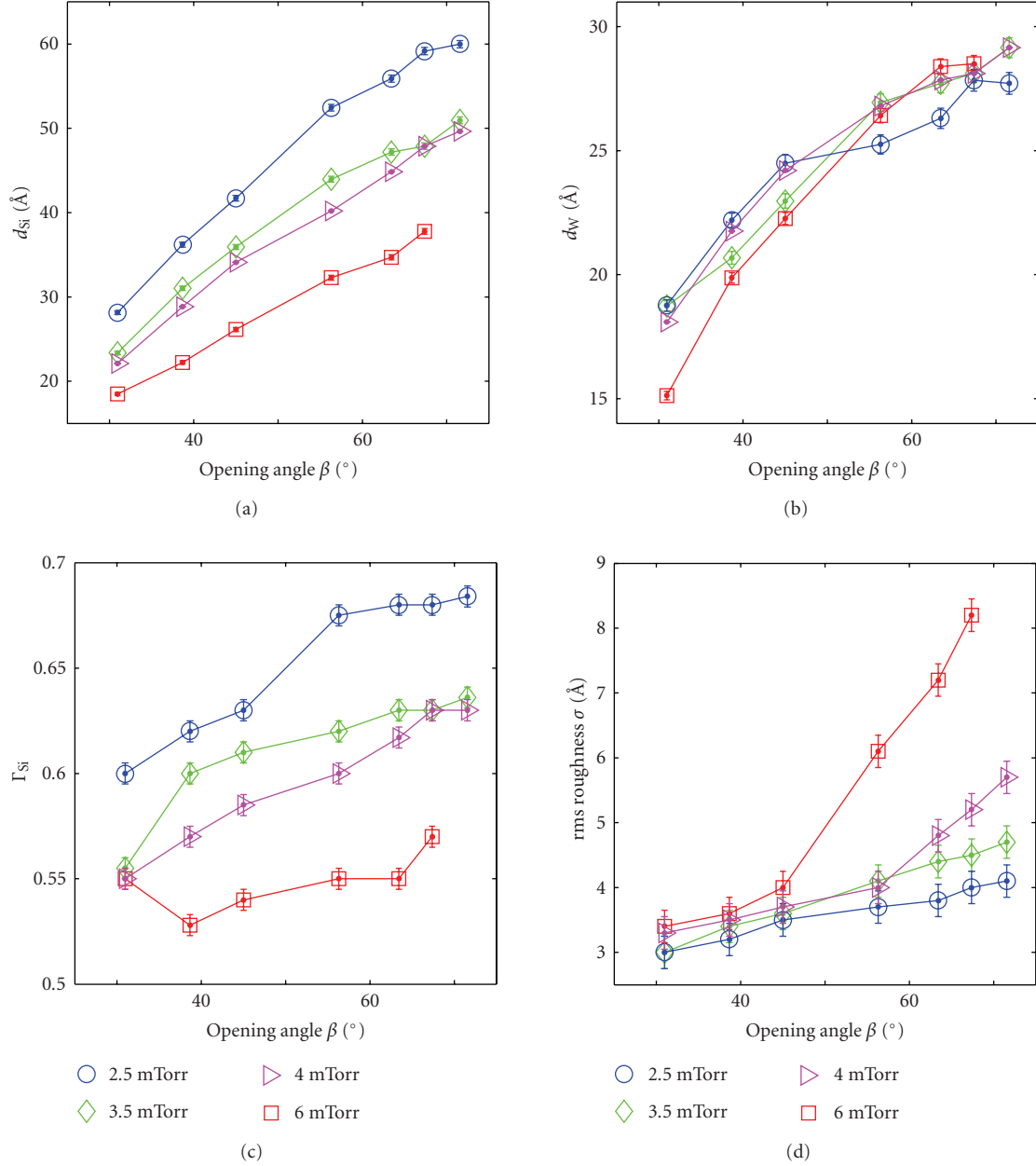
FIGURE 3: Data from specular reflectivity measurements of multilayers comprised of 10 bilayers of W/Si. The substrates are commercially available Si wafers with an rms roughness of about 2.75 Å. For 4 different pressures of Ar, the viewgraphs show (a) and (b) the thickness of Si and W versus the opening angle β. (c) The fraction of Si Γ_{Si} versus the opening angle β. (d) The rms roughness versus the opening angle β.

and a substrate during coating. The target is standing vertical and the arrows symbolize the particles ejected from the target on their way to the substrate shown to the right. The dashed vertical line indicates the honeycomb mesh which provides the collimation and prevents the material symbolized with the red arrows from reaching the substrate. As shown in the top-view sketch, the substrate may be mounted with an angle τ to the mounting plate. The degree of collimation is described either by the solid angle spanned by the mesh or the opening angle θ_{MAX}. θ_{MAX} is defined as follows: 99% of the particles which reaches the substrate has been

ejected from the target with a polar angle smaller θ_{MAX}. In the horizontal direction, the opening angle of the chimney around the target is $\pm 51°$. This method of collimation preserves the homogeneity defined by the target, that is, there is no shadowing effect associated with these collimators. The honeycomb mesh is mounted on the chimney of each target (rather than on the mounting plates), hence there is no patterning of the substrate from the mesh. Given the distance between the target and the mesh, the degree of collimation is dependent on the honeycomb cell diameter and mesh thickness, see Table 1. The honeycomb is electrically floating
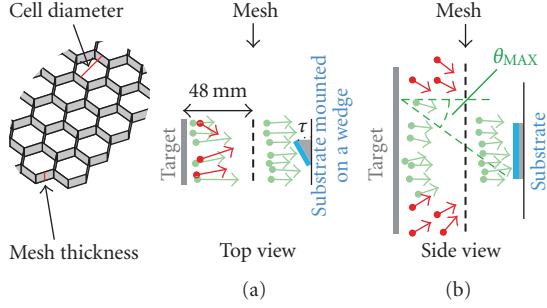
FIGURE 4: (Left) Sketch of the honeycomb mesh. (a) A top view of the coating geometry. Here, the flat substrate is mounted on a wedge defined by the angle τ. The wedges are designed so the distance between the target and substrate center is independent of the value of τ. (b) A side-view sketch of the coating geometry with $\tau = 0$.

and is placed between the plasma and the substrate, so no sputtering of the honeycomb occurs.

3.2.2. Experiment II

An experiment has been performed to investigate the relationship between the angle of incidence of the sputtered material and the rms roughness. At the DNSC sputtering facility, substrates were coated with predefined angles τ to the target, see Figure 4(a). The angles were $\{0.0, 3.7, 6.3, 16.3, 23.7, 26.3, 33.7, 36.3, 43.7\}°$. The collimation of the sputtered material was provided by mesh type 1 (see Table 1) in order to get as narrow an angular distribution of the particles incident on the substrates. The substrates were coated with one layer of W on an Si substrate, and the mean thickness of the coating was 244 Å. The coating thickness is dependent on $\cos\tau$, where the $\tau = 0°$ coating has at thickness of 269 Å and the $\tau = 43.7°$ coating has a thickness of 220 Å. Figure 5 shows that the rms roughness is fairly constant up to $\tau = 30°$. For $\tau > 30°$, the rms roughness is growing at an increasing rate. Similar experimental results are reported on in [6].

3.2.3. Experiment III

The main purpose of this experiment is to identify which mesh is the optimal collimator for the sputtering facility at DNSC, that is, a collimator which suppress the roughness and preserves an acceptable coating rate. Further the coating rate associated with each mesh type has been determined and compared to the mesh geometry in order to estimate an ejection law. We have produced multilayers with 6 different honeycomb mesh collimators, see Table 1. The Si substrates were mounted with $\tau = 0$ and the multilayers are comprised of 10 bilayers of W/Si.

The circular data points of Figure 6 indicate the rms roughness of the multilayers versus the solid angle spanned by the honeycomb mesh collimators (lower x-axis) and θ_{MAX} (upper x-axis). The data shows that magnetron sputtering with mesh types 1–4 as collimators results in multilayers with similar low roughness. A collimation provided by the large
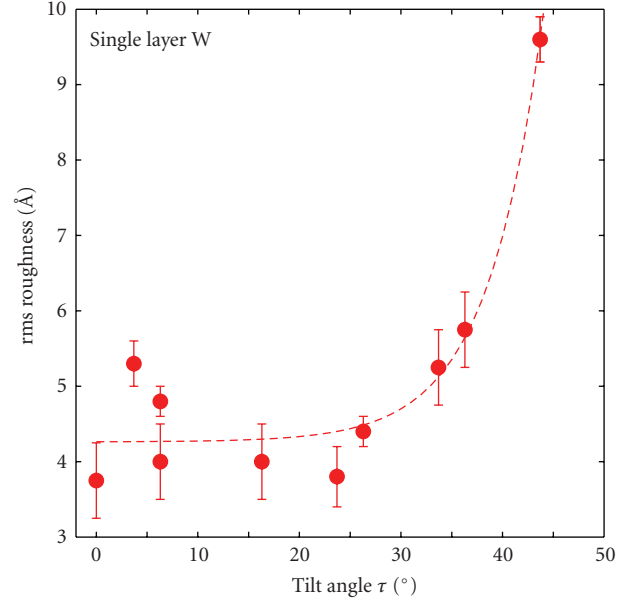

FIGURE 5: The rms roughness versus the tilt angle τ.

solid angle mesh of types 5-6 results in multilayers with a larger rms roughness.

The square data points indicate the coating rate associated with each of the 6 meshes. Not surprisingly, there is a different coating rate associated with each mesh, that is, a collimation with a more transparent mesh results in a bigger coating rate. The collimation with a large solid angle (type 6) reduces the coating rate to approximately 50% of the coating rate when there is no collimation at all.

The data show that an increase of the collimation beyond that provided by mesh type 4 will not affect the rms roughness noteworthy. In order not to decrease the coating rate unnecessarily the collimation provided by mesh type 4 is chosen as the optimal collimator for flat mirrors in the current geometry.

3.2.4. Estimation of the Angular Distribution of Particles Ejected from the Target

Based on the knowledge of the coating rate associated with each mesh and the mesh geometry, an *ejection law*, that is the angular distribution of particles ejected from the target, is estimated. We follow the approach first presented in [7]. From the ejection law so derived, we calculate the *intensity of sputtered particles which arrive at the substrate* versus the polar angle of ejection. In the following, the angular distribution of particles incident on the substrate $\mathcal{I}(\theta)$ is estimated from a simple model which neglects the scattering of the particles on, that is, the Ar ions/atoms. This means that the particles ejected from the target are assumed to follow a linear path to the substrate. This is a good approximation only for the W atoms. Further, the model does not consider the effects of resputtering and backscattering from the surface of the substrate. We adopt

TABLE 1: The solid angle spanned by the honeycomb mesh mounted the distance $\mathcal{L}_H$ = 48 mm from the target.

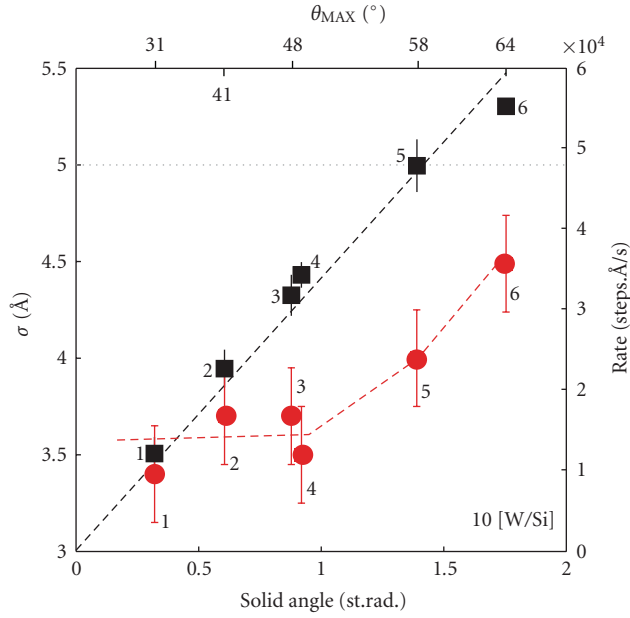| Mesh type	1	2	3	4	5	6
Mesh thickness (mm)	**10**	**10**	**10**	**5**	5	5
Cell diameter (mm)	**6.4**	**9.6**	**12.8**	**6.4**	9.6	12.8
Solid angle (st.rad.)	**0.32**	**0.61**	**0.88**	**0.92**	1.4	1.8
θ_{MAX} (°), $P(\theta) = \mathcal{C}$	**31**	**41**	**48**	**49**	58	64
θ_{MAX} (°), $P(\theta)$ defined by (1), α = 1.15	**31**	**41**	**48**	**48**	57	62

FIGURE 6: The mesh is mounted 48 mm from the target. The circular data points show the rms roughness σ of multilayers comprised of 10 bilayers of W/Si; the dashed red line is a guide to the eye. The multilayers have been produced with different degrees of collimation provided by honeycomb mesh of types 1–6, see Table 1. The number next to each data point refers to the mesh type in Table 1 and the gray dashed line indicates the rms roughness of a [W/Si] multilayer mirror produced with no collimation at all. The lower x-axis indicates the total solid angle spanned by the mesh while the upper x-axis indicates the value of θ_{MAX} (see text). The square data points indicate the coating rate associated with each mesh.

the model previously suggested in [7, 8] for the angular distribution $P(\alpha, \theta)$ of particles ejected from the target,

$$P(\alpha, \theta) = \frac{2\cos\alpha}{\alpha^2 + (1 - \alpha^2)\cos^2\theta}. \tag{1}$$

Here, θ is the polar angle and the value of the parameter α determines the angular width of $P(\alpha, \theta)$. As indicated in the insets of Figure 7, the expression for $P(\alpha, \theta)$ is derived by considering an ellipse: the parameter α is the ratio of the major to minor axis of the ellipse, and $P(\alpha, \theta)$ is the length of a vector with a direction specified by θ. Ideally, the angular distribution of particles ejected from each target should be considered independently. However, following the approach adopted in [7], here is considered an efficient
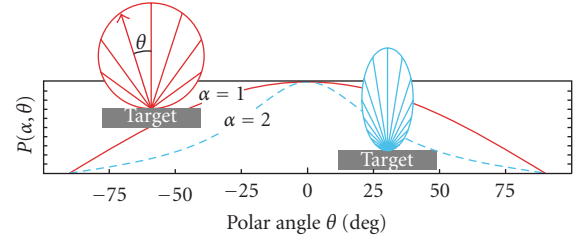

FIGURE 7: The angular distribution $P(\alpha, \theta)$ of particles ejected from a point on the target (1). The insets show two different top views of the target during sputtering. The length of the vector with the direction specified by θ is a measure of the amount of material ejected in that direction. In both cases shown, the intensity of ejected particles is strongest in the forward direction toward the substrate and decreases with increasing angle θ.
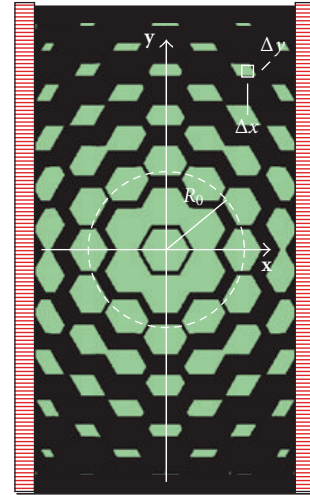

FIGURE 8: The view from the point $(0,0)$ at the target through a honeycomb mesh. (see text).

angular distribution of the two materials (W and Si) together. In [7], a value of α = 1 is estimated for the material combination Mo/Si.

First, the solid angle Φ_{tot} spanned by a honeycomb mesh is calculated. For this calculation, it is convenient to define a coordinate-system oriented as shown in Figure 8. Further it is convenient to define a function $\mathcal{T}(x, y, \mathcal{L}_H)$ which describes the transparency of a given mesh which is placed the distance $\mathcal{L}_H$ from the target. This function assumes the value 1 if the mesh is transparent (corresponding to the green areas of Figure 8) and 0 otherwise.

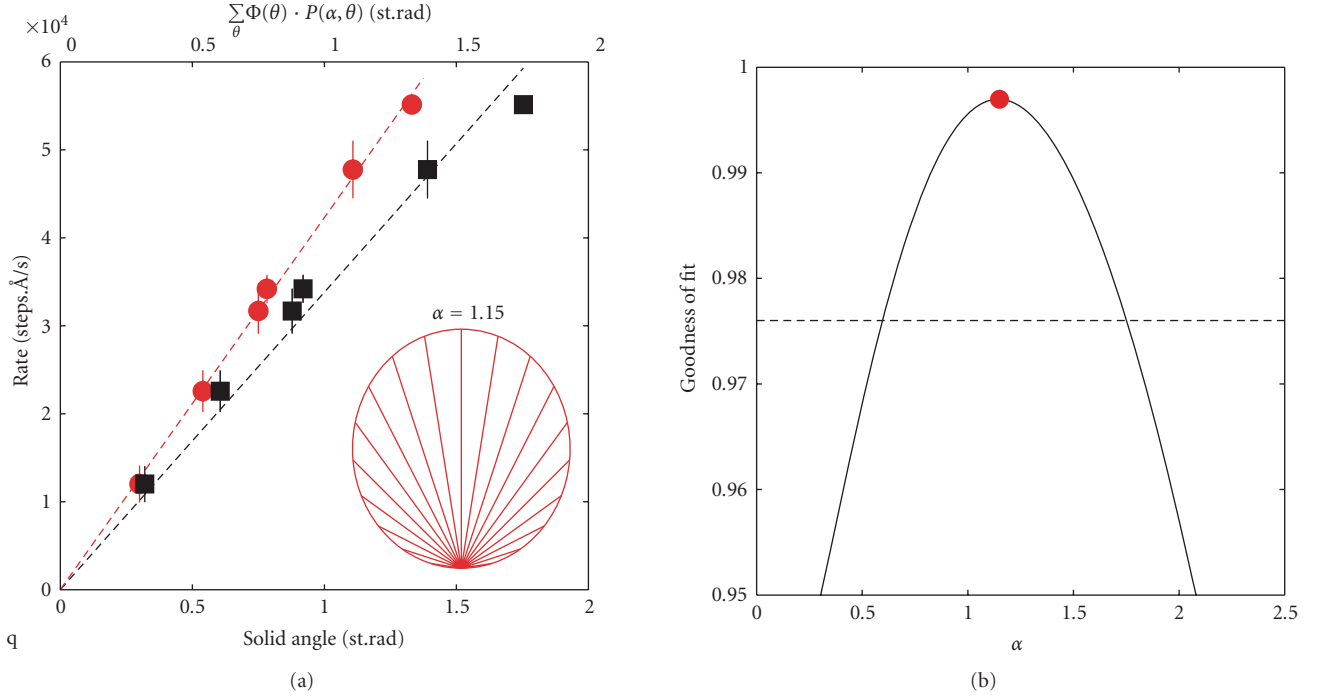q   (a)   (b)

FIGURE 9: (a) The coating rate increases with the total solid angle. The black square data points indicate the coating rate versus the solid angle (lower X-axis), and the black dashed line is a linear fit assuming that $P(\theta) = \mathcal{C}$ in (5). The red circles show the coating rate versus the sum over theta of $\Phi(\theta)P(\alpha,\theta)$ (5) with $\alpha = 1.15$ (upper X-axis). (b) The goodness of the linear fits (GOF) of the coating rate to (5) versus the parameter α. The dashed line indicates GOF for $P(\theta) = \mathcal{C}$. The red circle marks the maximum of GOF corresponding to the value $\alpha = 1.15$.

For the remaining calculations, it is practical to calculate the solid angle in the following way: the points (x, y) of a circle with the center at $(0, 0)$ are sharing the same polar angle θ, that is, the dashed circle of **Figure 8** corresponds to the polar angle $\theta_0 = \arccos(\mathcal{L}_H / \sqrt{R_0^2 + \mathcal{L}_H^2})$. The number of particles ejected from the point $(0, 0)$ at the target which are transmitted with the angle θ_0 is then proportional to $\Phi(\theta_0)$, where

$$\Phi(\theta_0) = \sum_{(x,y)\,|\,\sqrt{x^2+y^2}=R_0} \mathcal{T}(x, y) \frac{\Delta x\,\Delta y}{(\mathcal{L}_H/\cos\theta_0)^2}, \tag{2}$$

and the total solid angle is then calculated according to

$$\Phi_{\text{tot}} = \sum_\theta \Phi(\theta). \tag{3}$$

Note that $\Phi(\theta)$ is defined with a point of origin at $(0, 0)$. Since not only this point but *all* points (x, y) of the target contribute with ejected particles, the number of particles per time $\mathcal{l}(\theta)$ transmitted through the mesh is calculated as an average over all points of the target,

$$\mathcal{l}(\theta) \propto P(\alpha, \theta)\langle\Phi(\theta)\rangle_{\text{target}}. \tag{4}$$

Within this model the coating rate is proportional to

$$\sum_\theta \mathcal{l}(\theta) \propto \sum_\theta P(\alpha, \theta)\langle\Phi(\theta)\rangle_{\text{target}}. \tag{5}$$

The coating rate has been determined experimentally for the 6 honeycomb mesh in question, and the function

$\Phi(\theta)$ is determined (numerically) from the geometry of each mesh according to (2). This means that we are now in a position to estimate the ejection law $P(\alpha, \theta)$ for the material combination W/Si by using α as a fitting parameter.

It is worth noting that if the angular distribution of particles ejected from the target could be described by $P(\theta) = \mathcal{C}$, where $\mathcal{C}$ is a constant, the coating rate associated with one mesh would be directly proportional to the solid angle Φ_{tot} spanned by that mesh. The black squares of **Figure 9(a)** show the coating rate versus the spanned solid angle Φ_{tot} (the lower X-axis). The dashed line is a linear fit y to the data points Y. Figure 9(b) compares the goodness of the fits (GOF) defined as

$$\text{GOF} = 1 - \frac{\sum_i (Y_i - y_i)^2}{\sum_i (Y_i - \langle Y \rangle)^2}. \tag{6}$$

Here, $(Y_i - y_i)$ is the deviation of one data point Y_i from the fit y_i and $(Y_i - \langle Y \rangle)$ is the deviation of one data point from a horizontal line through mean value of all the data points. The dashed line indicates the goodness of the linear fit to the coating rate versus Φ_{tot}, and the solid line indicates GOF versus the parameter α. The best fit is obtained with $\alpha = 1.15$.

3.2.5. Estimation of the Transmitted Intensity versus Polar Angle

Figure 10 shows the transmitted particle intensity $\mathcal{l}(\theta)$ versus the polar angle θ as defined in (4). The view graphs
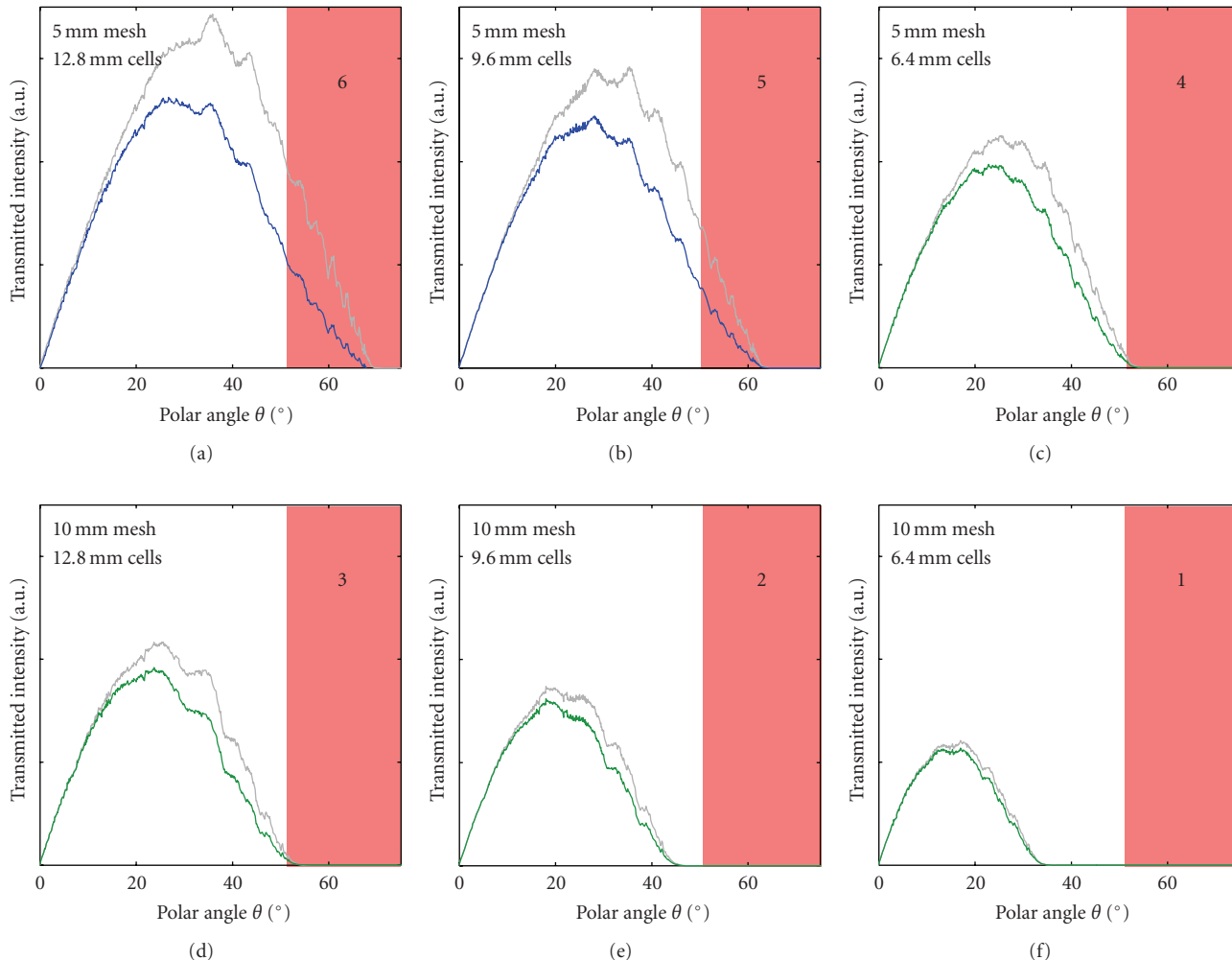
FIGURE 10: The number of sputtered particles transmitted through the mesh versus the polar angle θ calculated according to (4). The green and blue curves are calculated with $P(\alpha, \theta)$ described by (1) with $\alpha = 1.15$. The gray curves are calculated with $P(\theta) = \mathcal{C}$.

compare $\mathcal{I}(\theta)$ calculated with the assumption of $P(\alpha = 1.15, \theta)$ with $\mathcal{I}(\theta)$ calculated with $P(\alpha, \theta) = \mathcal{C}$. These curves have maximum between $\sim 15°$ (type 1) and $\sim 30°$ (type 6) and FWHM in the range from $\sim 22°$ (type 1) to $\sim 40°$ (type 6). The red regions mark the range of angles which is excluded by the separator plate collimation when the distance between the plates is 60 mm and the plates are 50 mm wide. From the six curves, only the blue ones have tails inside the red areas which indicate the range $\theta > 51°$. The curves indicate that the angular particle distribution of the DNSC system is strongly dependent on the properties of the honeycomb collimator. As shown in Figure 6, magnetron sputtering with a collimation provided by the mesh of types 5 and 6 results in multilayers with a relatively large rms roughness compared to that obtained with the mesh types 1–4.

Table 1 compares the values of θ_{MAX} calculated with the two different models for the angular distribution of particles ejected from the target, namely, $P(\alpha, \theta) = \mathcal{C}$ and $P(\alpha, \theta)$ defined by (1) with $\alpha = 1.15$. As expected from Figure 10, the two different models for $P(\theta)$ give similar results for θ_{MAX}.

4. Summary

At the sputtering facility of DNSC, it has been shown that the collimation of the sputtered particles plays an important role in the production of W/Si multilayers with low rms roughness. Two methods of collimation have been presented, they are referred to as the separator plate collimation and the honeycomb mesh collimation, respectively.

In experiments I and III [W/Si] multilayers were produced by DC-magnetron sputtering with different degrees of collimation of the sputtered particles. In experiment I we used the separator plate collimation, whereas the honeycomb mesh collimation was used in experiment III. In both experiments we saw that the multilayers produced with collimators opaque for sputtered particles with polar angles exceeding $\sim 50°$ have similar low (3.5 Å rms) interface roughness. When particles with polar angles above $\sim 50°$ are allowed to pass on to the substrate, a strong increase of the interface roughness is observed. Regarding the honeycomb mesh collimation, for each mesh the particle flux versus the polar angle has been estimated from the mesh geometry. For

the sputtering facility at DNSC, the mesh of type 4 is the optimal collimator, since this mesh suppresses the roughness and has the highest coating rate.

In experiment II single layers of W were deposited on Si substrates. Here, the sputtered particles were collimated by mesh type 1, which is the mesh spanning the smallest solid angle and hence providing the most narrow particle flux distribution versus the polar angle. The substrates were mounted on wedges defining the angle τ to the target. It is important to note that the angle of incidence of the particles on the substrate is not defined by τ alone: the particle flux allowed by mesh type 1 is centered around $15°$ and has a width of approximately $22°$. We observed a strong increase of the roughness for $\tau > \sim 35°$. Taking into account that the maximum particle flux is at a polar angle of $15°$, this is in correspondence with the results of experiments I and III.

The honeycomb mesh collimators qualify the sputtering chamber for the coating of low-roughness multilayer mirrors. The length of the substrates which can be coated at DNSC is now limited only by the length of the targets. By utilizing this new type of collimators, DNSC has produced the multilayer mirrors for an optical element [9] for the next generation X-ray source, the compact light source [4].

References

[1] C. P. Jensen, K. K. Madsen, H. C. Chen, F. E. Christensen, and E. Ziegler, "Coating of the HEFT telescope mirrors: method and results," in *X-Ray and Gamma-Ray Telescopes and Instruments for Astronomy*, J. E. Truemper and H. D. Tananbaum, Eds., vol. 4851 of *Proceedings of SPIE*, pp. 724–733, Waikoloa, Hawaii, USA, August 2002.

[2] J. E. Koglin, F. E. Christensen, W. W. Craig, et al., "NuSTAR hard X-ray optics," in *Optics for EUV, X-Ray, and Gamma-Ray Astronomy II*, O. Citterio and S. L. O'Dell, Eds., vol. 5900 of *Proceedings of SPIE*, pp. 266–275, San Diego, Calif, USA, August 2005.

[3] C. P. Jensen, K. K. Madsen, A. Jensen, and F. E. Christensen, "W/SiC and Pt/SiC multilayers for the NuSTAR hard x-ray telescope," in *Optics for EUV, X-Ray, and Gamma-Ray Astronomy II*, O. Citterio and S. L. O'Dell, Eds., vol. 5900 of *Proceedings of SPIE*, pp. 40–46, San Diego, Calif, USA, August 2005.

[4] http://www.lynceantech.com/.

[5] S. M. Rossnagel, D. Mikaelsen, H. Kinoshita, and J. J. Cuomo, "Collimated magnetron sputter deposition," *Journal of Vacuum Science & Technology A*, vol. 9, no. 2, pp. 261–265, 1991.

[6] J. Dalla Torre, G. H. Gilmer, D. L. Windt, et al., "Microstructure of thin tantalum films sputtered onto inclined substrates: experiments and atomistic simulations," *Journal of Applied Physics*, vol. 94, no. 1, pp. 263–271, 2003.

[7] D. M. Broadway, Y. Ya. Platonov, and L. A. Gomez, "Achieving desired thickness gradients on flat and curved substrates," in *X-Ray Optics, Instruments, and Missions II*, R. B. Hoover and A. B. C. Walker, Eds., vol. 3766 of *Proceedings of SPIE*, pp. 262–274, Denver, Colo, USA, July 1999.

[8] J. L. Vossen, "A sputtering technique for coating the inside walls of through-holes in substrates," *Journal of Vacuum Science and Technology*, vol. 11, no. 5, pp. 875–877, 1974.

[9] A. Jensen, *Optical elements for hard X-ray radiation*, Ph. D. Thesis, Niels Bohr Institute, Faculty of Science, University of Copenhagen, Copenhagen, Denmark, 2007.

Special Issue on
High-Power Fiber Lasers and Applications

Call for Papers

Over the past few years, the power produced by fiber laser systems has been rapidly increasing, rising to a technological revolution in the field of solid-state lasers. Continuous wave fiber lasers are the most powerful solid-state laser technology available today: they are able to provide diffraction-limited power on the order of several kilowatts. Fiber lasers are even more promising in view of the practicality for use: their monolithic, compact, and efficient technological platforms can be produced in a very different way from the complicated assembly processes typically required for the production of conventional bulk solid-state lasers. The combination of high power and ease of use could benefit applications in a wide variety of fields, including semiconductor device manufacturing, medical surgery, directed energy platforms, material processing, laser spectroscopy, remote sensing and imaging, and scientific instrumentation.

The breakthrough in fiber lasers has been driven by many key factors related to progress in new optical materials, novel designs, innovative photonic theories and in the development of high-brightness semiconductor diode pumps. For example, the emergence of double-clad and large mode area (LMA) fibers has contributed to the achievement of higher laser powers in three ways: by reducing the detrimental effects of nonlinear interactions in the core, by reducing the fiber damage possibility, and by allowing the use of higher pump powers. Motivated by application requirements, the development of fiber lasers has become very diverse (e.g., high output power, narrow linewidth, broad band, short pulse, eye safe wavelengths, Raman amplifiers, etc.). This special issue will focus on reporting those recent progresses in this exciting area.

For this special issue, both original research and tutorial reviewing articles are solicited in the following areas:

- New photonic materials for high-power fiber lasers and amplifiers
- New fiber laser and amplifier designs
- Novel techniques for beam combining (coherent, spectral, incoherent)
- Optical nonlinearity and noise; stimulated Brillouin scattering mitigation
- Photodarkening effects
- Design and fabrication of photonic crystal and bandgap fibers
- Supercontinuum generation in fibers
- Photonic components for high-power fiber lasers
- Nonlinear frequency conversion in fiber lasers
- Discussions on future trends and challenges

Before submission, authors should carefully read over the journal's Author Guidelines, which are located at http://www.hindawi.com/journals/aoe/guidelines.html. Prospective authors should submit an electronic copy of their complete manuscript through the journal Manuscript Tracking System at http://mts.hindawi.com/, according to the following timetable:

Manuscript Due	October 1, 2009
First Round of Reviews	January 1, 2010
Publication Date	April 1, 2010

Lead Guest Editor

Yalin Lu, Laser and Optics Research Center, Department of Physics, US Air Force Academy, CO 80840, USA; yalin.lu@usafa.edu

Guest Editors

Thomas Seefeld, BIAS Bremer Institut für angewandte Strahltechnik GmbH, Klagenfurter Straße 2, 28359 Bremen, Germany; seefeld@bias.de

Iyad Dajani, High Power Solid State Lasers Branch, Air Force Research Laboratory, 3550 Aberdeen SE, Kirtland AFB, 87117 NM, USA; iyad.dajani@kirtland.af.mil

Pierre Bourdon, Theoretical and Applied Optics Department, ONERA, the French Aerospace Lab, Chemin de la Huniere, 91761 Palaiseau Cedex, France; pierre.bourdon@onera.fr

Special Issue on
X-Ray Focusing: Techniques and Applications

Call for Papers

This Special Issue of the Journal of X-Ray Optics and Instrumentation is devoted to a broad coverage of the increasingly important topic of X-ray focusing, including optics, beams, and applications. In part, this effort is a followup on a successful 2008 SPIE Optics and Photonics workshop on the same topic, with the goal of a comprehensive review of the topic in an archival form. Focused X-ray beams, ranging in size from nanometers to micrometers, are needed for a broad range of applications, from biology to material sciences, to interrogate physical, chemical, and biological states and processes with ever finer spatial resolution. In X-ray astronomy, improved focusing optical systems are needed for imaging faint or new objects. This Special Issue covers the latest in X-ray focusing techniques including theory, development, limitations, progress, and applications in a single archival document.

Topics to be covered in this Special Issue include, but are not limited to:

- Micro- and nanofocusing techniques (mirrors, multilayer, lenses, crystals, zone plates, polycapillaries, Kinoform arrays, multipore, etc.)
- Theory and computations
- Metrology
- Implementation (mounting, etc.)
- Feedback and control
- Applications

Before submission authors should carefully read over the journal's Author Guidelines, which are located at http://www.hindawi.com/journals/xroi/guidelines.html. Prospective authors should submit an electronic copy of their complete manuscript through the journal Manuscript Tracking System at http://mts.hindawi.com/ according to the following timetable:

Manuscript Due	November 1, 2009
First Round of Reviews	February 1, 2010
Publication Date	May 1, 2010

Lead Guest Editor

Ali Khounsary, Advanced Photon Source, Argonne National Laboratory, Argonne, IL 60439, USA; amk@aps.anl.gov

Guest Editors

Gene Ice, Materials Science and Technology Division, Oak Ridge National Laboratory, Oak Ridge, TN 37831-6118, USA; icege@ornl.gov